Characterization of the seismic response of gas-hydrate bearing sediments

Juan E. Santos[1,2,3], Patricia M. Gauzellino[4], José M. Carcione[5], and Jing Ba[1]

[1]School of Earth Sciences and Engineering, Hohai University, Nanjing, 211100, China

[2]Universidad de Buenos Aires, Facultad de Ingeniería, Instituto del Gas y del Petróleo, Av. Las Heras 2214 Piso 3, C1127AAR Buenos Aires, Argentina

[3]Department of Mathematics, Purdue University, 150 N. University Street, West Lafayette, Indiana, 47907-2067, USA

[4]Departamento de Geofísica Aplicada, Facultad de Ciencias Astronómicas y Geofísicas, Universidad Nacional de La Plata, Paseo del Bosque s/n, La Plata, B1900FWA, Argentina

[5]Istituto Nazionale di Oceanografia e di Geofisica Sperimentale (OGS), Borgo Grotta Gigante 42c, 34010 Sgonico, Trieste, Italy

Key Points:

- Gas-hydrate bearing sediments are modeled as a composite materials consisting of the rock frame and gas-hydrates saturated by water.
- An upscaling finite element procedure is used to determine effective viscoelastic media long-wave equivalent to heterogeneous gas-hydrate bearing sediments.
- The composite model predicts that local variations in gas-hydrate concentration (ice content) induce high velocity dispersion and attenuation on P- and S- waves.

Corresponding author: Jing Ba, baj04@mails.tsinghua.edu.cn

Abstract

Gas-hydrate bearing sediments are composite materials consisting of two weakly-coupled porous solid phases and a fluid phase. The solid phases are the rock frame and gas-hydrates, consisting of an ice-like lattice of water molecules with gas molecules, mostly methane, trapped inside. These composite media have heterogeneities at multiple mesoscopic scales, which induce velocity dispersion and attenuation of seismic waves within a broad range of frequencies. These effects can be explained by mode conversions and wave induced fluid flow (WIFF). This work presents time-harmonic compressibility and shear experiments to determine effective complex plane-wave and shear moduli for the composite material. These moduli define an effective isotropic viscoelastic medium long-wave equivalent to an heterogeneous gas-hydrate bearing porous rock. The experiments are defined as boundary value problems that are solved using the Finite Element (FE) method. The procedure is applied to composite media with regions of different ice content of fractal or periodic layered distribution. The examples demonstrate that variations in ice content induce strong attenuation and dispersion effects on seismic waves due to the WIFF mechanism.

1 Introduction

Gas-hydrate bearing sediments are partially frozen porous rocks containing heterogeneities at multiple mesoscopic scales. These structures consist of a water phase and two non-welded solid phases, the porous skeleton and gas-hydrates, which are ice-like lattices of water molecules with gas molecules trapped inside (Ecker et al. (2000), Guerin and Goldberg (2005)). The interest in these formations, located in permafrost and seafloor continental margins, is based on their influence on global climate change and geohazards (Lee and Collet (2001), Lee (2002), Carcione and Tinivella (2000)). Furthermore, they are considered as future potential energy resources (Ecker et al. (2000). Leclaire et al (1994) presented a Biot-type three-phase theory based on first principles. The theory, valid for uniform porosity, predicts three compressional waves and two shear waves and can be applied to unconsolidated and consolidated porous media.The observation of additional slow waves was presented by Leclaire et al (1995). Carcione and Seriani (1998) designed a generalization of this theory to evaluate gas-hydrate concentration. The extension of the theory of Leclaire et al. (1994) to the variable porosity case was presented by Carcione et al. (2003) and Santos et al. (2004). Wave simulation in partially frozen porous media was presented by Carcione and Seriani (2001) and Carcione et al. (2003).

When fast compressional or shear waves travel through these materials, regions with different ice content suffer different strains and fluid pressures. This in turn generates wave induce fluid flow (WIFF) and diffusive Biot slow waves causing energy losses and velocity dispersion (mesoscopic loss mechanism). White et al. (1975) and coauthors were the first to model the wave-induced fluid flow caused by mesoscopic-scale heterogeneities, showing that this mechanism causes important attenuation and velocity dispersion effects at seismic frequencies in partially saturated rocks.

Using a numerical approach to model wave propagation in gas-hydrate bearing sediments would allow to model heterogeneities of any kind and shape. However, this methodology would be computationally expensive or even not feasible due to different reasons. First, very fine meshes would be needed to represent the heterogeneities. In addition, in the low frequency range the diffusion length is very small as compared with the seismic wavelengths, and must be properly discretized to represent the fluid pressure equilibration. To overcome this limitations, we propose the use of a numerical upscaling procedure to determine an *effective viscoelastic isotropic medium* (EVIM) long-wave equivalent to a highly heterogeneous gas-hydrate bearing sediment.

The EVIM is determined using time-harmonic compressibility and shear experiments to numerical rock samples at a finite number of harmonic frequencies. The com-

plex plane-wave and shear moduli defining the EVIM are defined using the solution of two boundary value problems (BVP's). These BVP's are formulated in the space-frequency domain using the equations for composite materials derived by Santos et al. (2004) with appropriate boundary conditions, and are solved using a FE procedure. The EVIM determined in this fashion has in the average the same attenuation and velocity dispersion than the original gas-hydrate bearing porous rock.

For a detailed description of using harmonic experiments combined with FE procedures to determine the seismic response of Biot-type media with different types of heterogeneities we refer to Santos and Gauzellino (2017).

2 The differential model in the diffusive range of frequencies

Let Ω be an elementary cube of poroelastic material composed of two porous solid phases, referred to by the subscripts or superscripts 1 and 3, saturated by a single-phase fluid phase indicated by the subscript or superscript 2. Thus, $\Omega = \Omega_1 \cup \Omega_2 \cup \Omega_3$. Let V_i denote the volume of the phase Ω_i and V_b and V_{sm} the bulk volume of Ω and the solid matrix $\Omega_{sm} = \Omega_1 \cup \Omega_3$, so that

$$V_{sm} = V_1 + V_3, \qquad V_b = V_1 + V_2 + V_3.$$

Let $S_1 = \dfrac{V_1}{V_{sm}}$ and $S_3 = \dfrac{V_3}{V_{sm}}$ denote the two solid fractions of the composite matrix, respectively. The water content and the two solid fractions over the bulk material are defined as $\phi_w = \dfrac{V_2}{V_b}$, $\phi_1 = \dfrac{V_1}{V_b}$ and $\phi_3 = \dfrac{V_3}{V_b}$, respectively, so that $\phi_1 + \phi_w + \phi_3 = 1$.

Note that ϕ_w is the effective porosity, and not the porosity when the rock is completely unfrozen. The latter is the absolute of actual porosity ϕ_a, given by $\phi_a = \phi_w + \phi_3 = 1 - \phi_1$.

The ice content I' is defined as $I' = \dfrac{\phi_3}{1 - \phi_w}$, so that $0 \le I' \le 1$.

Let $\mathbf{u}^{(1)}$, $\mathbf{u}^{(2)}$ and $\mathbf{u}^{(3)}$ be the averaged solid and fluid displacements over the bulk material. Let $\boldsymbol{\tau}^{(1)} = (\tau_{ij}^{(1)})$ and $\boldsymbol{\tau}^{(3)} = (\tau_{ij}^{(3)})$ denote the stress tensors in Ω_1 and Ω_3 averaged over the bulk material Ω, respectively, and let p_f denote the fluid pressure. These quantities describe small changes with respect to reference values corresponding to an initial equilibrium state. Next we introduce the tensors

$$\tau_{jk}^{(1,T)} = \tau_{jk}^{(1)} - S_1 \phi p_f \delta_{jk}, \qquad \tau_{jk}^{(3,T)} = \tau_{jk}^{(3)} - S_3 \phi p_f \delta_{jk}, \tag{1}$$

associated with the total stresses in Ω_1 and Ω_3 averaged over the bulk material, respectively. The relative fluid displacement is defined as

$$\mathbf{w} = \phi_w \big(\mathbf{u}^{(2)} - S_1 \mathbf{u}^{(1)} - S_3 \mathbf{u}^{(3)} \big), \tag{2}$$

with $\zeta = -\nabla \cdot \mathbf{w}$ representing the change in fluid content. Furthermore, let

$$\epsilon_{ij}(u^{(m)}) = \frac{1}{2} \left(\frac{\partial u_i^{(m)}}{\partial x_j} + \frac{\partial u_j^{(m)}}{\partial x_i} \right), \quad m = 1, 3,$$

denote the strain tensor in Ω_m with linear invariant $\theta_m = \epsilon_{ii}(u^{(m)})$.

In the diffusive range of frequencies and in the absence of body forces, the constitutive relations and diffusive equations for a partially frozen porous medium are (Santos et al. (2004))

$$\tau_{jk}^{(1,T)} = \big[K_{G1} \theta_1 - B_1 \zeta + B_3 \theta_3 \big] \delta_{jk} + 2\mu_1 d_{jk}^{(1)} + \mu_{1,3} d_{jk}^{(3)}, \tag{3}$$

$$\tau_{jk}^{(3,T)} = \big[K_{G3} \theta_3 - B_2 \zeta + B_3 \theta_1 \big] \delta_{jk} + 2\mu_3 d_{jk}^{(3)} + \mu_{1,3} d_{jk}^{(1)}, \; j,k = 1,2,3, \tag{4}$$

$$p_f = -B_1 \theta_1 - B_2 \theta_3 + M \zeta, \tag{5}$$

$$\mathrm{i}\omega \mathrm{f}_{11}\mathbf{u}^{(1)} - \mathrm{i}\omega \mathrm{f}_{12}\mathbf{u}^{(2)} - \mathrm{i}\omega \mathrm{f}_{11}\mathbf{u}^{(3)} = \nabla \cdot \boldsymbol{\tau}^{(1,\mathrm{T})}, \tag{6}$$

$$-\mathrm{i}\omega \mathrm{f}_{12}\mathbf{u}^{(1)} + \mathrm{i}\omega \mathrm{f}_{22}\mathbf{u}^{(2)} + \mathrm{i}\omega \mathrm{f}_{12}\mathbf{u}^{(3)} = -\nabla \mathrm{p}_{\mathrm{f}}, \tag{7}$$

$$-\mathrm{i}\omega \mathrm{f}_{11}\mathbf{u}^{(1)} + \mathrm{i}\omega \mathrm{f}_{12}\mathbf{u}^{(2)} + \mathrm{i}\omega \mathrm{f}_{11}\mathbf{u}^{(3)} = \nabla \cdot \boldsymbol{\tau}^{(3,\mathrm{T})}. \tag{8}$$

where ω is the angular frequency and $\mathrm{i} = \sqrt{-1}$.

The elastic coefficients in equations (3)–(5) and the diffusive coefficients f_{11}, f_{22} and f_{12} in equations (6)-(8) can be determined in terms of the material properties of the solid and fluid phases as explained in Santos et al. (2004), Appendices A and B.

3 Determination of the complex P-wave and S-wave moduli of the equivalent viscoelastic medium

Let us denote by $\mathcal{T}(\widetilde{\mathbf{u}}^s)$ and $\mathcal{E}(\widetilde{\mathbf{u}}^s)$ the stress and strain tensors of the EVIM, and set $\widetilde{\Theta}^s = \nabla \cdot \widetilde{\mathbf{u}}^s$, where $\widetilde{\mathbf{u}}^s$ denotes the solid displacement vector at the macroscale. The constitutive equations of the EVIM, stated in the space-frequency domain, are

$$\mathcal{T}_{jk}(\widetilde{\mathbf{u}}^s) = \overline{\lambda}\widetilde{\Theta}^s \delta_{jk} + 2\overline{\mu}\mathcal{E}_{jk}(\widetilde{\mathbf{u}}^s). \tag{9}$$

Next we will show a procedure to determine the complex modulus $\overline{E_u} = \overline{\lambda} + 2\overline{\mu}$ and the complex shear modulus $\overline{\mu}$ in gas-hydrate bearing sediments. For this purpose, we solve the diffusive equations (6)-(8) in the 2D case on a reference square $\Omega = (0, L)^2$ in the (x_1, x_3)-plane with boundary $\Gamma = \Gamma^L \cup \Gamma^B \cup \Gamma^R \cup \Gamma^T$, where Γ^L, Γ^R, Γ^T and Γ^B denote the left, right top and bottom boundaries of Γ. Denote by $\boldsymbol{\nu}$ the unit outer normal on Γ and let $\boldsymbol{\chi}$ be a unit tangent on Γ oriented counterclockwise.

To determine the complex modulus $\overline{E_u}$ we solve the diffusive equations (6)-(8) in Ω with the boundary conditions

$$\boldsymbol{\tau}^{(m,T)}(\mathbf{u})\boldsymbol{\nu} \cdot \boldsymbol{\nu} = -\Delta P_1, \quad (x_1, x_3) \in \Gamma^T, \quad m = 1, 3, \tag{10}$$

$$\boldsymbol{\tau}^{(m,T)}(\mathbf{u})\boldsymbol{\nu} \cdot \boldsymbol{\chi} = 0, \quad (x_1, x_3) \in \Gamma, \quad m = 1, 3, \tag{11}$$

$$\mathbf{u}^{(m)} \cdot \boldsymbol{\nu} = 0, \quad (x_1, x_3) \in \Gamma \setminus \Gamma^T, \quad m = 1, 3, \tag{12}$$

$$\mathbf{w} \cdot \boldsymbol{\nu} = 0, \quad (x_1, x_3) \in \Gamma. \tag{13}$$

In this experiment, $\epsilon_{11}(\mathbf{u}^{(1)}) = \epsilon_{13}(\mathbf{u}^{(1)}) = \epsilon_{11}(\mathbf{u}^{(3)}) = \epsilon_{13}(\mathbf{u}^{(3)}) = \nabla \cdot \mathbf{w} = 0$, so that $\mathcal{E}_{11}(\widetilde{\mathbf{u}}^s) = \mathcal{E}_{13}(\widetilde{\mathbf{u}}^s) = 0$ and (9) reduces to

$$\mathcal{T}_{33} = \overline{E_u}\mathcal{E}_{33}. \tag{14}$$

Now $\overline{E_u}$ can be determined from (14) by obtaining $\mathcal{T}_{33}$ and $\mathcal{E}_{33}$ as averages of the mesoscopic stress and strain tensors associated with the solid 1 phase over the sample Ω, i.e.,

$$\mathcal{T}_{33} = \frac{1}{\Omega}\int_\Omega \tau_{33}^{(1,T)} d\Omega, \qquad \mathcal{E}_{33} = \frac{1}{\Omega}\int_\Omega \epsilon_{33}^{(1)} d\Omega. \tag{15}$$

For obtaining the *equivalent* complex shear modulus $\overline{\mu}$, we solve (6)-(8) in Ω with the following boundary conditions

$$-\boldsymbol{\tau}^{(1,T)}(\mathbf{u})\boldsymbol{\nu} = \mathbf{g}_1, \quad (x_1, x_3) \in \Gamma^T \cup \Gamma^L \cup \Gamma^R, \tag{16}$$

$$-\boldsymbol{\tau}^{(3,T)}(\mathbf{u})\boldsymbol{\nu} = \mathbf{g}_3, \quad (x_1, x_3) \in \Gamma^T \cup \Gamma^L \cup \Gamma^R, \tag{17}$$

$$\mathbf{u}^{(m)} = 0, \quad (x_1, x_3) \in \Gamma^B, \quad m = 1, 3 \tag{18}$$

$$\mathbf{w} \cdot \nu = 0, \quad (x_1, x_3) \in \Gamma, \tag{19}$$

where

$$\mathbf{g}_1 = \begin{cases} (0, \Delta G_1), & (x_1, x_3) \in \Gamma^L, \\ (0, -\Delta G_1), & (x_1, x_3) \in \Gamma^R, \\ (-\Delta G_1, 0), & (x_1, x_3) \in \Gamma^T, \end{cases} \tag{20}$$

$$\mathbf{g}_3 = \begin{cases} (0, \Delta G_3), & (x_1, x_3) \in \Gamma^L, \\ (0, -\Delta G_3), & (x_1, x_3) \in \Gamma^R, \\ (-\Delta G_3, 0), & (x_1, x_3) \in \Gamma^T. \end{cases} \tag{21}$$

In this experiment, $\epsilon_{11}(\mathbf{u}^{(1)}) = \epsilon_{33}(\mathbf{u}^{(1)} = \epsilon_{11}(\mathbf{u}^{(3)}) = \epsilon_{33}(\mathbf{u}^{(3)} = \nabla \cdot \mathbf{w} = 0$ and consequently $\mathcal{E}_{11}(\widetilde{\mathbf{u}}^s) = \mathcal{E}_{33}(\widetilde{\mathbf{u}}^s) = 0$. Thus, (9) reduces to

$$\mathcal{T}_{13} = \overline{\mu}\mathcal{E}_{13}. \tag{22}$$

Next, $\overline{\mu}$ is determined from (22) by computing $\mathcal{T}_{13}$ and $\mathcal{E}_{13}$ by averaging the mesoscopic stress and strain tensors associated with the solid 1 phase over the sample Ω:

$$\mathcal{T}_{13} = \frac{1}{\Omega}\int_\Omega \tau_{13}^{(1)} d\Omega, \qquad \mathcal{E}_{13} = \frac{1}{\Omega}\int_\Omega \epsilon_{13}^{(1)} d\Omega. \tag{23}$$

The complex compressional and shear velocities are given by (Carcione, 2014)

$$v_{Pc}(\omega) = \sqrt{\frac{\overline{E_u}(\omega)}{\overline{\rho}}}, \quad v_{Sc}(\omega) = \sqrt{\frac{\overline{\mu}(\omega)}{\overline{\rho}}},$$

where $\overline{\rho}$ is the average bulk density of the sample, obtained as

$$\overline{\rho} = \phi_1\rho_1 + \phi_w\rho_2 + \phi_3\rho_3,$$

with $\rho_m, m = 1, 2, 3$ denoting the mass density of each solid and fluid constituent in Ω.

The effective compressional and shear phase velocities $v_n(\omega)$ and (inverse) quality factor $Q_n(\omega), n = P, S$ are determined using the relations (Carcione, 2014)

$$v_n(\omega) = \left[\mathrm{Re}\left(\frac{1}{v_{nc}(\omega)}\right)\right]^{-1}, \qquad \frac{1}{Q_n(\omega)} = \frac{\mathrm{Im}(v_{nc}(\omega)^2)}{\mathrm{Re}(v_{nc}(\omega)^2)}, \quad n = P, S. \tag{24}$$

The approximate solution (6)-(8) with the boundary conditions (10)–(13) to determine $\overline{E_u}$ and and (16)– (19) to determine $\overline{\mu}$ was obtained using the FE procedure described in Appendix B.

4 Numerical experiments

To validate the procedure, we consider a water saturated homogeneous square sample of side length 10 cm discretized using a 80×80 uniform mesh. Absolute porosity is $\phi_a = 0.3$. The material properties of solid 1, solid 3 (ice) and water are given in Table 1.

The effective phase velocities v_n and dissipation factors $1000/Q_n$, $n = P, S$ obtained using the harmonic experiments for the composite model were validated by comparison against those corresponding to the associated classic Biot model defined in Appendix A and using plane-wave analysis.

4.1 Validation varying ice content at 50 Hz and varying frequency for ice content $I' = 0.333$

Table 2 shows the results for the effective P-wave phase velocities at 50 Hz varying the ice content. Its comparison with the values of the associated classic Biot model is displayed in the column of the percentual error. The error decreases with decreasing ice content. We consider that this is due to the very different elastic behavior of the solid 1 and solid 3 (ice) phases.

Furthermore, the effective P-wave velocities as a function of frequency for ice content I'=0.333 were computed in the range 1 Hz–1 kHz. We obtained a constant effective P-wave velocity of 3992.67 m/s and numerical ∞ for the quality factor Q. We also computed the P-wave velocity for the associated classic Biot model defined in Appendix A using a plane-wave analysis, obtaining a constant of 4087.86 and dissipation factors in the range $10^{-2} - 10^{-5}$.

An analog to Table 2 is presented in the Table 3 for the results of the effective S-wave phase velocities.

Table 3 shows that, as for P-waves, errors decrease with decreasing ice content. We also computed the effective S-wave velocities as a function of frequency for ice content I'=0.333. In the frequency range 1 Hz–1 kHz we obtained an effective S-wave velocity of 2476.96 m/s and numerical ∞ for the shear quality factor Q. The plane-wave analysis for the associated classical Biot model gives an S-wave phase velocity of 2477.85 m/s, while the dissipation factors are in the range $10^{-2} - 10^{-5}$.

5 Effective P-wave phase velocity and dissipation factors in layered media with periodic variations in ice content I'

We consider a square sample of side length 18 cm size discretized with a 120×120 uniform mesh. The numerical sample has seven alternating layers of ice contents $I' = 0.666$ and I'= 0.166. Absolute porosity is $\phi_a = 0.3$.

To determine the FE approximations to the the plane wave modulus $\overline{E_u}(\omega)$, we solved the diffusive equations (6) – (8) with the boundary conditions (10)–(13) using the FE method for a finite number of frequencies in the range 1 Hz- 200 Hz.

The curves labeled *Associated classic Biot, theory* in Figures 1 and 2 were obtained as follows. First we determined the associated classic Biot model for each layer of the periodic sequence as indicated in Appendix A. Then, we use the theory presented by Krzikalla and Müller (2011) to obtain the theoretical values.

Figure 1 exhibits effective P-wave phase velocities for the composite model increasing with increasing, while those of the associated classic Biot model are almost constant in the whole range of frequencies. Furthermore, in almost all the frequency range the composite model exhibits lower effective velocities than the classic model, due to the high dispersion induced by the WIFF mechanism. Figure 2 displays the effective dissipation factor of the composite model, where it can be observed the strong attenuation of P-waves due to the interlayer WIFF mechanism, with an attenuation peak of quality factor $Q = 80$ at about 70 Hz. Figure 3 displays the logarithm of the dissipation factor for the composite and associated classic Biot models, where attenuation is negligible for the associated classic Biot model.

Figures 4 and 5 show the gradient of fluid pressure for this experiment at 10 Hz and 70 Hz, where their higher values can be observed at the interlayer boundaries and are due to variations in ice content in the sample. These Figures illustrates the WIFF mechanism. Furthermore, these gradients are much higher at 70 Hz than at 10 Hz, in accordance with Figure 2.

6 Patchy ice-content.

Gas-hydrate bearing sediments have local variations in ice content I' at multiple mesoscopic scales. To model wave propagation in this type of medium, a convenient approach is to use an EVIM as defined in the previous sections. This EVIM takes into account the WIFF and the associated dispersion and attenuation effects.

To generate binary multiscale quasi-fractal heterogeneities in ice content I' we use a stochastic fractal field based on the von Karman self-similar correlation function with spectral density (Frankel and Clayton (1986))

$$S_d(k_{x_1}, k_{x_3}) = S_0(1 + k^2 a^2)^{-(H+N_e/2)} \tag{25}$$

where $k = \sqrt{k_{x_1}^2 + k_{x_3}^2}$ is the radial wave-number, N_e is the Euclidean dimension, a the correlation length, H is a self-similarity coefficient ($0 < H < 1$) and S_0 is a normalization constant. Equation (25) corresponds to a fractal process of dimension $D = N_e + 1 - H$ at scales smaller than a.

We consider a water-saturated square sample Ω of side length 10 cm and a 80×80 uniform mesh, so that $\Omega = \cup\Omega_j^J$. First, a pseudo-random number is assigned to each Ω_j. This random field is Fourier transformed to the spatial wave-number domain and its spectrum is multiplied by the spectrum in (25). The result is transformed back to the spatial domain to obtain a micro-heterogeneous ice content model I'_j. Then choosing an appropriate threshold value $I_j'^*$ we construct a sample with multi-scale highly-heterogeneous binary quasi-fractal distribution I' and a desired overall ice content.

Figures 6 and 7 display the patchy ice content distribution I' for correlation lengths 3.33 cm and 2.22 cm, respectively. Fractal dimension is D = 2.2, and overall ice content I' is 36 %. Figure 8 shows the Lamé shear coefficient μ_1 associated with the patchy ice content distribution I' in Figure 2, where the local heterogeneities in μ_1 are due to the local variations in the ice content. Figures 9 and 10 show effective phase velocities and logarithm of the dissipation factors of P-waves as a function of frequency for the composite and classic Biot models in the range 0.01 Hz–140 Hz and binary ice content I' as in Figure 6 (correlation length 3.33 cm). The results for the classic Biot model were obtained using the FE upscaling procedure presented by Santos et al. (2009).

As in the periodic layered case, P-wave velocities for the composite model are lower than those of the associated classic Biot model, show highly dispersive behavior and higher values with increasing frequency, while those of the associated classic Biot model are almost constant in all the frequency range.

Figure 10 shows that attenuation of P-waves is much higher for the composite model than for the associated classic Biot model. This attenuation mechanism, due to the induced WIFF effect, is not present when the associated classic Biot model is used. Figure 11 exhibits dissipation factors as a function of frequency for the harmonic composite model and the binary ice content distributions in Figures 6 and 7. Two attenuation peaks are clearly observed. The peak located at low frequencies corresponds to the larger ice patches (Figure 6).

Next, we analyze the behavior of the effective shear waves as a function of frequency due to variations in ice content. In this case, we consider a square sample of side length 1 cm with a multiscale quasi-fractal patchy ice content distribution. The patches have ice content $I' = 0.666$ and $I' = 0.166$. Absolute porosity is $\phi_a = 0.3$, correlation length is 0.04 cm and fractal dimension is $D = 2.2$. Overall ice content is 41 %. Figure 12 displays the shear Lamé coefficient associated with this quasi-fractal ice content distribution. It is observed that S-waves suffer very little velocity dispersion, as can be seen in Figure 13, and negligible attenuation. We also computed the corresponding effective phase velocity and dispersion coefficient of the associated classic Biot model, obtaining a constant shear phase velocity of 2428 m/s and negligible attenuation.

7 Conclusions

The numerical upscaling procedure presented in this work determines effective complex and frequency dependent P- and S- wave moduli associated with a heterogeneous gas-hydrate bearing poroelastic medium. These moduli define an effective viscoelastic isotropic medium long-wave equivalent to the heterogeneous gas-hydrate bearing medium. The methodology is applied to the seismic response of water saturated poroelastic samples for the cases of periodic alternating layers or patches of different ice content. The analysis shows that local variations in ice content induce high velocity dispersion and attenuation for P- waves traveling in gas-hydrate bearing sediments, while S-waves are less sensitive to these type of heterogeneities.

8 Appendix A

In this appendix, we explain a procedure to determine the elastic and dissipative factors of an associated classic Biot model that in the low-frequency range is *equivalent* to a composite material. The following notation is used to define the associated classical Biot model (Biot, 1962).

Let $\widehat{\mathbf{u}}^{(s)}, \widehat{\mathbf{u}}^{(f)}$ denote the solid and fluid displacement vectors and set $\widehat{\theta}^{(m)} = \nabla \cdot \widehat{\mathbf{u}}^{(m)}, m = s, f$. Also, let $\widehat{\boldsymbol{\sigma}}$ and $\widehat{p}_f$ denote the total stress and fluid pressure.

In the diffusive range of frequencies and in the absense of body forces, the constitutive relations and the diffusion equation of the classic Biot model for a fluid saturated poroelastic medium can be stated as

$$\widehat{\sigma}_{ij} = \left[K_G \widehat{\theta}^{(s)} - B\widehat{\theta}^{(f)}\right]\delta_{ij} + 2\mu \widehat{d}_{ij}^{(s)}, \tag{26}$$

$$\widehat{p}_f = -B\widehat{\theta}^{(s)} - \widehat{M}\widehat{\theta}^{(f)}, \tag{27}$$

$$\nabla \cdot \widehat{\boldsymbol{\sigma}} = 0, \tag{28}$$

$$i\omega \frac{\eta}{\widehat{\kappa}} \widehat{\mathbf{u}}^{(f)} + \nabla p_f = 0, \tag{29}$$

where

$$\widehat{d}_{ij}^{(s)} = \epsilon_{ij}(\widehat{\mathbf{u}}^{s)}) - \frac{1}{3}\widehat{\theta}^{(s)}\delta_{ij}.$$

In (26)- (29), K_G and μ are the bulk and shear moduli of the saturated material, while B and M are coupling coefficients between the solid and fluid phases. Furthermore, $\widehat{\kappa}$ denotes the effective permeability.

Assume that $\mathbf{u}^{(1)} = \mathbf{u}^{(3)} \equiv \mathbf{u}^{(s)}$ (the low-frequency assumption is used here) and define the total stress tensor as

$$\tau_{ij} = \tau_{ij}^{(1,T)} + \tau_{ij}^{(3,T)}. \tag{30}$$

Then adding (3) and (4), we obtain

$$\begin{aligned} \tau_{ij} = \big[&(K_{G1} + K_{G3} + 2\ B_3)\,\theta^{(s)} - (B_1 + B_2)\,\theta^{(f)}]\delta_{ij} \\ &+2\,(\mu_1 + \mu_3\mu_{13})\,d_{ij}^{(s)}, \end{aligned} \tag{31}$$

$$p_f = -(B_1 + B_2)\theta(s) - M\theta(f), \tag{32}$$

Now from (26), (27) and (31), (32), we can identify the elastic coefficients of the associated classic Biot model as follows:

$$K_G = K_{G1} + K_{G3} + 2\ B_3, \tag{33}$$

$$B = B_1 + B_2, \tag{34}$$

$$\mu = \mu_1 + \mu_3 + \mu_{13}, \tag{35}$$

$$\widehat{M} = M. \tag{36}$$

The procedure to determine the coefficients K_G, B, M and μ in (33)- (36) can be shown to give identical results than when they are computed as presented in Carcione et al. (2005). .

Furthermore, from equation (B5) and (B8) in Santos et al. (2004)

$$\phi\left(S_3\phi f_{22} - f_{12}\right) = b_{23}, \tag{37}$$

$$\phi\left(f_{12} + S_1\phi f_{22}\right) = b_{12}, \tag{38}$$

where

$$b_{12} = \phi^2\frac{\eta}{\kappa_1}, \qquad b_{23} = \phi^2\frac{\eta}{\kappa_3}, \tag{39}$$

Hence multiplying (37) and (38) by ϕ and adding the resulting equations we obtain

$$f_{22} = \eta\left(\frac{1}{\kappa_1} + \frac{1}{\kappa_3}\right). \tag{40}$$

Next, from the low-frequency assumption, the f_{12}-terms in (7) cancel and this equation reduces to

$$i\omega f_{22}\mathbf{u}^{(2)} + \nabla p_f = 0. \tag{41}$$

Thus (29), (40) and (41) allow to identify the *effective* permeability $\widehat{\kappa}$ of the associated classic Biot model by the relation

$$\frac{1}{\widehat{\kappa}} = \left(\frac{1}{\kappa_1} + \frac{1}{\kappa_3}\right). \tag{42}$$

Equations (33)-(36) and (42) completely define the associated classic Biot media to our composite material.

Remark: Equations (33)-(36) and (42) may also be used in the case of shaley sandstones as presented in Santos et al. (2004).

9 Appendix B

10 A variational formulation

To state a variational formulation, we first introduce some notation. For $X \subset \mathbb{R}^d$ with boundary ∂X, let $(\cdot,\cdot)_X$ and $\langle\cdot,\cdot\rangle_{\partial X}$ denote the complex $L^2(X)$ and $L^2(\partial X)$ inner products for scalar, vector, or matrix valued functions. Also, for $s \in \mathbb{R}$, $\|\cdot\|_{s,X}$ denotes the usual norm in the Sobolev space $H^s(X)$, with the subscript X being omitted if $X = \Omega$ or $X = \Gamma$.

In the analysis that follows we need the following closed subspaces of $[H^1(\Omega)]^2$:

$$\mathcal{W}^P(\Omega) = \{\mathbf{v} \in [H^1(\Omega)]^2 : \mathbf{v}\cdot\boldsymbol{\nu} = 0 \text{ on } \Gamma \setminus \Gamma^T\},$$

$$\mathcal{W}^S(\Omega) = \{\mathbf{v} \in [H^1(\Omega)]^2 : \mathbf{v} = 0 \text{ on } \Gamma^B\}.$$

Also, let us introduce the functional spaces

$$H_0(\mathrm{div};\Omega) = \{\mathbf{v} \in H(\mathrm{div};\Omega) : \mathbf{v}\cdot\boldsymbol{\nu} = 0 \text{ on } \Gamma\},$$

$$H^1(\mathrm{div};\Omega) = \{\mathbf{v} \in [H^1(\Omega)]^2 : \nabla\cdot\mathbf{v} \in H^1(\Omega)\}.$$

Furthermore, for $(I) = (P, S)$ let

$$\mathcal{Z}^I(\Omega) = \mathcal{W}^I(\Omega) \times H_0(\mathrm{div};\Omega) \times \mathcal{W}^I(\Omega)\ .$$

To obtain a variational formulation associated with $\overline{E_u}(\omega)$, take $\mathbf{v} = \left(\mathbf{v}^{(1)}, \mathbf{v}^{(2)}, \mathbf{v}^{(3)}\right) \in \mathcal{Z}^P(\Omega)$ Then multiply equations (6) by $\mathbf{v}^{(1)}$, equation (7) by $\mathbf{v}^{(2)}$ and equation (8) by $\mathbf{v}^{(3)}$, integrate by parts using the boundary conditions (10)-(13) and add the resulting equations to get *the variational formulation*: find $\mathbf{u}^{(P)} = (\mathbf{u}^{(1,P)}, \mathbf{u}^{(2,P)}, \mathbf{u}^{(3,P)}) \in \mathcal{Z}^P(\Omega)$ such that

$$
\begin{aligned}
&\Lambda(\mathbf{u}^{(P)}, \mathbf{v}) = \mathrm{i}\omega \left(\mathrm{f}_{11}\mathbf{u}^{(1,\mathrm{P})} - \mathrm{f}_{12}\mathbf{u}^{(2,\mathrm{P})} - \mathrm{f}_{11}\mathbf{u}^{(3,\mathrm{P})}, \mathbf{v}^{(1)}\right) \\
&+\mathrm{i}\omega \left(-\mathrm{f}_{12}\mathbf{u}^{(1,\mathrm{P})} + \mathrm{f}_{22}\mathbf{u}^{(2,\mathrm{P})} + \mathrm{f}_{12}\mathbf{u}^{(3,\mathrm{P})}, \mathbf{v}^{(2)}\right) \\
&+\mathrm{i}\omega \left(-\mathrm{f}_{11}\mathbf{u}^{(1,\mathrm{P})} + \mathrm{f}_{12}\mathbf{u}^{(2,\mathrm{P})} + \mathrm{f}_{11}\mathbf{u}^{(3,\mathrm{P})}, \mathbf{v}^{(3)}\right) \\
&+\sum_{pq} \left(\tau_{pq}^{(1,T)}(\mathbf{u}^{(P)}),\, \varepsilon_{pq}(\mathbf{v}^{(1)})\right) - \left(p_f(\mathbf{u}^{(P)}), \nabla \cdot \mathbf{v}^{(2)}\right) \\
&+\sum_{pq} \left(\tau_{pq}^{(3,T)}(\mathbf{u}^{(P)}),\, \varepsilon_{pq}(\mathbf{v}^{(3)})\right) \\
&= -\left\langle \Delta P_1, \mathbf{v}^{(1)} \cdot \boldsymbol{\nu} \right\rangle_{\Gamma^T} - \left\langle \Delta P_3, \mathbf{v}^{(3)} \cdot \boldsymbol{\nu} \right\rangle_{\Gamma^T}, \quad \forall \quad \mathbf{v} = \left(\mathbf{v}^{(1)}, \mathbf{v}^{(2)}, \mathbf{v}^{(3)}\right) \in \mathcal{Z}^P(\Omega).
\end{aligned}
\tag{43}
$$

Similarly, to obtain our variational formulation associated with $\overline{\mu}(\omega)$, take $\mathbf{v} = \left(\mathbf{v}^{(1)}, \mathbf{v}^{(2)}, \mathbf{v}^{(3)}\right) \in \mathcal{Z}^S(\Omega)$. Then multiply equations (6) by $\mathbf{v}^{(1)}$, equation (7) by $\mathbf{v}^{(2)}$and equation (8) by $\mathbf{v}^{(3)}$, integrate by parts using the boundary conditions (16)-(19) and add the resulting equations to get *the variational formulation*: find $\mathbf{u}^{(S)} = (\mathbf{u}^{(1,S)}, \mathbf{u}^{(2,S)}, \mathbf{u}^{(3,S)}) \in \mathcal{Z}^S(\Omega)$ such that

$$
\begin{aligned}
&\Lambda(\mathbf{u}^{(S)}, \mathbf{v}) = \mathrm{i}\omega \left(\mathrm{f}_{11}\mathbf{u}^{(1,\mathrm{S})} - \mathrm{f}_{12}\mathbf{u}^{(2,\mathrm{S})} - \mathrm{f}_{11}\mathbf{u}^{(3,\mathrm{S})}, \mathbf{v}^{(1)}\right) \\
&+\mathrm{i}\omega \left(-\mathrm{f}_{12}\mathbf{u}^{(1,\mathrm{S})} + \mathrm{f}_{22}\mathbf{u}^{(2,\mathrm{S})} + \mathrm{f}_{12}\mathbf{u}^{(3,\mathrm{S})}, \mathbf{v}^{(2)}\right) \\
&+\mathrm{i}\omega \left(-\mathrm{f}_{11}\mathbf{u}^{(1,\mathrm{S})} + \mathrm{f}_{12}\mathbf{u}^{(2,\mathrm{S})} + \mathrm{f}_{11}\mathbf{u}^{(3,\mathrm{S})}, \mathbf{v}^{(3)}\right) \\
&+\sum_{pq} \left(\tau_{pq}^{(1,T)}(\mathbf{u}^{(S)}),\, \varepsilon_{pq}(\mathbf{v}^{(1)})\right) - \left(p_f(\mathbf{u}^{(S)}), \nabla \cdot \mathbf{v}^{(2)}\right) \\
&+\sum_{pq} \left(\tau_{pq}^{(3,T)}(\mathbf{u}^{(S)}),\, \varepsilon_{pq}(\mathbf{v}^{(3)})\right) \\
&= \left\langle \mathbf{g}_1, \mathbf{v}^{(1)} \right\rangle_{\Gamma \setminus \Gamma^B} + \left\langle \mathbf{g}_3, \mathbf{v}^{(3)} \right\rangle_{\Gamma \setminus \Gamma^B}, \quad \forall \quad \mathbf{v} = \left(\mathbf{v}^{(1)}, \mathbf{v}^{(2)}, \mathbf{v}^{(3)}\right) \in \mathcal{Z}^S(\Omega).
\end{aligned}
\tag{44}
$$

An existence and uniqueness result for the solution of problems (43) and (44) is presented in Santos and Carcione (2015).

11 Finite element formulation

Let $\mathcal{T}^h(\Omega)$ be a non-overlapping partition of Ω into rectangles Ω_j of diameter bounded by h such that $\overline{\Omega} = \cup_j^J \overline{\Omega}_j$. Denote by $\Gamma_{jk} = \partial\Omega_j \cap \partial\Omega_k$ the common side of two adjacent rectangles Ω_j and Ω_k. Also, let $\Gamma_j = \partial\Omega_j \cap \Gamma$.

We employ the space of globally continuous piecewise bilinear polynomials to approximate each component of the solid displacements $\mathbf{u}^{(1)}$ $\mathbf{u}^{(3)}$, while the vector part of the Raviart-Thomas-Nedelec space of zero order is used to approximate the fluid displacement vector $\mathbf{u}^{(2)}$ (Raviart and Thomas (1977), Nedelec (1980)). More specifically, let

$$
\mathcal{W}^{h,P}(\Omega) = \{\mathbf{v} : \mathbf{v}|_{\Omega_j} \in [P_{1,1}(\Omega_j)]^2,\ \mathbf{v} \cdot \boldsymbol{\nu} = 0 \text{ on } \Gamma \setminus \Gamma^T\} \cap [C^0(\overline{\Omega})]^2,
$$

$$
\mathcal{W}^{h,S}(\Omega) = \{\mathbf{v} : \mathbf{v}|_{\Omega_j} \in [P_{1,1}(\Omega_j)]^2,\ \mathbf{v} \cdot \boldsymbol{\nu} = 0 \text{ on } \Gamma^B\} \cap [C^0(\overline{\Omega})]^2,
$$

be the Finite Element (FE) space to approximate the solid displacement vectors $\mathbf{u}^{(1)}$ and $\mathbf{u}^{(3)}$, and let

$$\mathcal{V}^h(\Omega) = \{\mathbf{v} \in H(\mathrm{div};\Omega) : \mathbf{v}|_{\Omega_j} \in P_{1,0}(\Omega_j) \times P_{0,1}(\Omega_j),\ \mathbf{v}\cdot\boldsymbol{\nu} = 0 \text{ on } \Gamma\}$$

be the FE space to approximate the fluid displacement vector $\mathbf{u}^{(2)}$. Here $P_{s,t}$ denotes the polynomials of degree not greater than s in x_1 and not greater than t in x_3.

Next, for $(I) = (P, S)$ let

$$\mathcal{Z}^{h,I}(\Omega) = \mathcal{W}^{h,I}(\Omega) \times \mathcal{V}^h(\Omega) \times \mathcal{W}^{h,I}(\Omega).$$

Now, we formulate the FE procedures to determine $\overline{E_u}$ and $\overline{\mu}$:

- $\overline{E_u}(\omega)$: find $\mathbf{u}^{(h,P)} \in \mathcal{Z}^{h,P}(\Omega)$ such that

$$\Lambda(\mathbf{u}^{(h,P)}, \mathbf{v}) = -\left\langle \Delta P_1, \mathbf{v}^{(1)}\cdot\boldsymbol{\nu}\right\rangle_{\Gamma^T} - \left\langle \Delta P_3, \mathbf{v}^{(3)}\cdot\boldsymbol{\nu}\right\rangle_{\Gamma^T},\ \forall\ \mathbf{v} \in \mathcal{Z}^{h,P}(\Omega) \quad (45)$$

- $\overline{\mu}(\omega)$: find $\mathbf{u}^{(h,S)} \in \mathcal{Z}^{h,S}(\Omega)$ such that

$$\Lambda(\mathbf{u}^{(h,S)}, \mathbf{v}) = \left\langle \mathbf{g}_1, \mathbf{v}^{(1)}\right\rangle_{\Gamma\setminus\Gamma^B} + \left\langle \mathbf{g}_3, \mathbf{v}^{(3)}\right\rangle_{\Gamma\setminus\Gamma^B}, \qquad \forall\ \mathbf{v} \in \mathcal{Z}^{h,S}(\Omega), \quad (46)$$

  where $\mathbf{g}_1$ and $\mathbf{g}_3$ are defined in (20)-(21).

It was shown in Santos and Carcione (2015) that the error associated with the FE procedures (45) and (46) is on the order $O(h^{1/2})$ in the H^1- norm.

Next we briefly describe the local basis to represent the solid displacements $\mathbf{u}^{(1)}, \mathbf{u}^{(3)}$ and the fluid displacement vector $\mathbf{u}^{(2)}$ on a reference rectangle $\widehat{R} = [0,1]^2$.

For the solid displacements we consider a local basis of bilinear polynomials $\mathcal{V}(\widehat{R})$, defined as

$$\mathcal{V}(\widehat{R}) = \mathrm{Span}\{\varphi^{BL},\ \varphi^{BR},\ \varphi^{TR},\ \varphi^{TL}\},$$

where φ^{BL} is a bilinear polynomial taking the value one at the bottom left corner of $\widehat{R}$ and vanishing at the other three corners of $\widehat{R}$, and similarly for the other three basis functions.

For the fluid displacement vector $\mathbf{u}^{(2)}$ we choose four degrees of freedom associated with its normal component at the mid points $\xi^l, l = L, R, B, T$ of the faces of $\widehat{R}$. Thus, defining the local basis

$$\psi^L(x) = 1 - x,\ \psi^R(x) = x,\ \psi^B(z) = 1 - z,\ \psi^T(z) = z,$$

we have that

$$\mathcal{W}(\widehat{R}) = \mathrm{Span}\{(\psi^L(x), 0), (\psi^R(x), 0), (0, \psi^B(z)), (0, \psi^T(z))\}.$$

Our finite element approximations $\mathbf{U}^{(2)}$ to $\mathbf{u}^{(2)}$, $\mathbf{U}^{(1)} = (U_1^{(1)}, U_3^{(1)})$ to $\mathbf{u}^{(1)} = (u_1^{(1)}, u_3^{(1)})$ and $\mathbf{U}^{(3)} = (U_1^{(3)}, U_3^{(3)})$ to $\mathbf{u}^{(3)} = (u_1^{(3)}, u_3^{(3)})$ in the reference element $\widehat{R}$ are:

$$\begin{aligned}
\mathbf{U}^{(2)} &= U^L(\psi^L(x), 0) + U^R(\psi^R(x), 0) + U^B(0, \psi^B(z)) + U^T(0, \psi^T(z)),\\
\mathbf{U}_m^{(1)} &= U_m^{1,L}\varphi^{BL}(x,z) + U_m^{1,B}\varphi^{BR}(x,z) + U_m^{1,R}\varphi^{TR}(x,z) + U_m^{1,T}\varphi^{TL}(x,z),\\
\mathbf{U}_m^{(3)} &= U_m^{3,L}\varphi^{BL}(x,z) + U_m^{3,B}\varphi^{BR}(x,z) + U_m^{3,R}\varphi^{TR}(x,z) + U_m^{3,T}\varphi^{TL}(x,z),\ m = 1, 3,
\end{aligned}$$

By properly scaling the given basis elements we construct the spaces $\mathcal{V}^h$ and $\mathcal{W}^h$ used to represent the approximating functions $\mathbf{U}^{(1)}$, $\mathbf{U}^{(3)}$ and $\mathbf{U}^{(2)}$ for the solid and fluid displacement vectors on each element Ω_j.

Acknowledgments

This work was partially funded by ANPCyT, Argentina (PICT 2015 1909) and Universidad de Buenos Aires (UBACyT 20020160100088BA).

References

Biot, M. A. (1962). Mechanics of deformation and acoustic propagation in porous media. *Journal of Applied Physics*, 33, 1482-1498.

Carcione, J. M., & Seriani, G. (1998). Seismic velocities in permafrost. *Geophysical Prospecting*, 46 441–454.

Carcione, J. M., & Tinivella, U. (2000). Bottom-simulating reflectors: Seismic velocities and AVO effects. *Geophysics*, 65 (1) 54-67.

Carcione, J. M., & Seriani, G. (2001). Wave simulation in frozen porous media. *Journal of Computational Physics*, 170, 676-695.

Carcione, J. M., Santos, J. E., Ravazzoli, C. L., & Helle, H. B. (2003). Wave simulation in partially frozen porous media with fractal freezing conditions. *Journal of Applied Physics*, 94 (12) 7839-7847.

Carcione, J. M., Helle, H. B., Santos J. E., & Ravazzoli, C. L. (2005). A constitutive equation and generalized Gassmann modulus for multi-mineral porous media. *Geophysics*, 70 (2) N17–N26.

Carcione, J. M. (2014). Wave Fields in Real Media. Theory and numerical simulation of wave propa- gation in anisotropic, anelastic, porous and electromagnetic media, 3rd ed., extended and revised. Elsevier Science, Oxford.

Ecker, C., Dvorkin, J.,& Nur, A.M. (2000). Estimating the amount of gas hydrate and free gas from marine sediments. *Geophysics*, 65 (2) 565573.

Frankel, A., & Clayton, R. W. (1986). Finite difference simulation of seismic wave scattering: implications for the propagation of short period seismic waves in the crust and models of crustal heterogeneity. *Journal of Geophysical Research*, 91 6465–6489.

Guerin, G., & Goldberg, D. (2005). Modeling of acoustic wave dissipation in gas-hydrate bearing sediments. *Geochemistry, Geophysics, Geosystems*, 6 (7), doi:10.1029/2005GC000918.

Krzikalla, F., & Müller, T. M. (2011). Anisotropic P-SV-wave dispersion and attenuation due to interlayer flow in thinly layered porous rocks. *Geophysics*, 76 WA135.

Leclaire, P., Cohen-Tenoudji, F., & Aguirre Puente, J. (1994). Extension of Biots theory to wave propagation in frozen porous media. *Journal of the Acoustical Society of America*, 96 3753–3767.

Leclaire, P., Cohen-Tenoudji, F., & Aguirre Puente, J. (1995). Observation of two longitudinal and two transverse waves in a frozen porous medium. *Journal of the Acoustical Society of America*, 97 2052–2055.

Lee, M. W., & Collet, T. S. (2001). Elastic properties of gas hydrate-bearing sediments. *Geophysics*, 66 (3) 763-771.

Lee, M. W. (2002). Biot-Gassmann theory for velocities of gas hydrate-bearing sediments. *Geophysics*, 67 (6) 1711-1719.

Nedelec, J. C. (1980). Mixed finite elements in R^3. *Numerische . Mathematik*, 35 315-341.

Raviart, P. A., & Thomas, J. M. (1975). Mixed finite element method for 2nd order elliptic problems, Mathematical Aspects of the Finite Element Methods. *Lecture Notes of Mathematics*. 606 Springer.

Santos, J.E., Ravazzoli, C.L., & Carcione, J. M. (2004). A model for wave propagation in a composite solid matrix saturated by a single-phase fluid. *Journal of the Acoustical Society of America*, 115 (6) 2749-2760.

Santos, J. E., Ravazzoli, C. L., Gauzellino, P. M., & Carcione, J. M. (2009). A numerical upscaling procedure to estimate effective bulk and shear moduli in heterogeneous fluid-saturated porous media. *Computer Methods in Applied Mechanics and Engineering*, 198 2067-2077.

Santos, J. E., & Carcione, J. M. (2015). Finite-element harmonic experiments to model fractured induced anisotropy in poroelastic media. *Computer Methods in Applied Mechanics and Engineering*, 283 1189–1213.

Santos, J. E., & Gauzellino, P. M. (2017). *Numerical Simulation in Applied Geophysics*. Birkhauser, Lecture Notes in Geosystems Mathematics and Computing.

White, J. E., Mikhaylova, N. G., & Lyakhovitskiy, F. M. (1975). Low-frequency seismic waves in fluid saturated layered rocks. *Physics of the Solid Earth*, 11 654–659.

Table 1. Material Properties.

Solid grain	bulk modulus, K_{s1}	38.7 GPa
	shear modulus, μ_{s1}	39.6 GPa
	density, ρ_{s1}	2650 kg/m^3
	permeability κ_{s1}	1.07 10^{-13} m^2
Ice	bulk modulus, K_{s3}	8.58 GPa
	shear modulus, μ_{s3}	3.32 GPa
	density, ρ_{s3}	920 kg/m^3
	permeability κ_{s3}	5 10^{-4} m^2
Water	bulk modulus, K_f	2.25 GPa
	density, ρ_2	1040 kg/m^3
	viscosity, η	0.0018 Pa $\cdot$ s

391 **Table 2. Effective P-wave velocities (m/s) at 50 Hz as function of ice content**
392 **I'. The sample is square of side length 10 cm.**

Ice content I'	Composite model	Associated classic Biot model	Error (%)
0.666	4120.23	4291.95	4.0
0.583	4064.1868	4208.35	3.42
0.500	4027.02	4146.20	2.87
0.416	4004.44	4100.76	2.34
0.333	3992.67	4067.86	1.85
0.25	3988.476	4043.88	1.37
0.166	3989.24	4025.78	0.9

393

394 **Table 3. Effective S-wave phase velocities (m/s) at 50 Hz as function of ice**
395 **content I'. The sample is square of side length 10 cm.**

Ice content I'	Composite model	Associated classic Biot model	Error (%)
0.666	2627.56	2639.26	0.44
0.583	2627.56	2572.3665	0.28
0.500	2565.15	2526.03	0.16
0.416	2493.87	2495.93	0.08
0.333	2476.96	2477.85	0.03
0.25	2467.65	2467.95	0.01
0.166	2462.93	2462.99	0.0

396

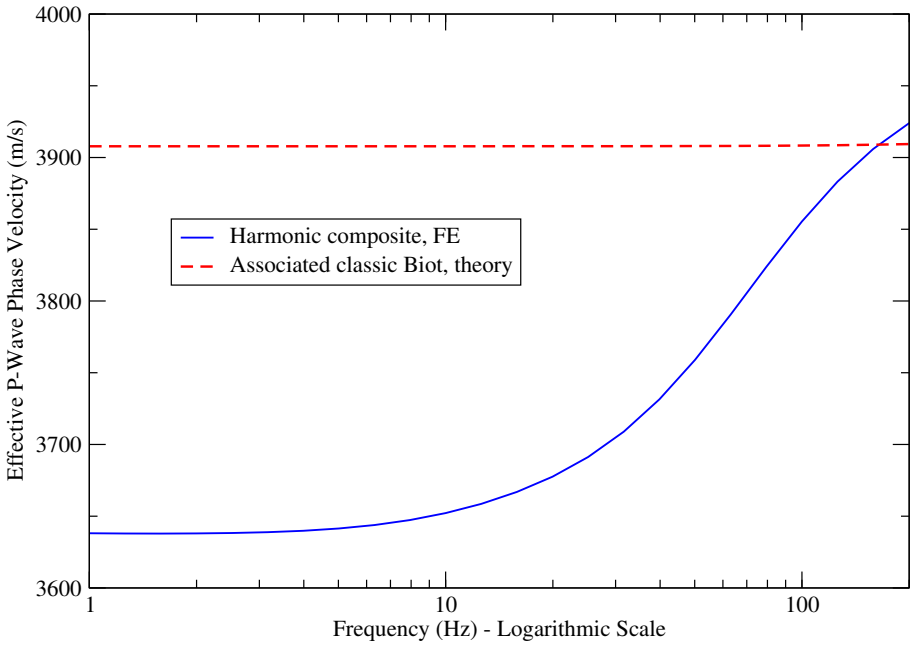

Figure 1. Effective P-wave phase velocity as a function of frequency for the composite and associated classic Biot models. The numerical sample is a square of side length 18 cm and has seven alternating layers of ice contents $I' = 0.666$ and $I' = 0.166$.

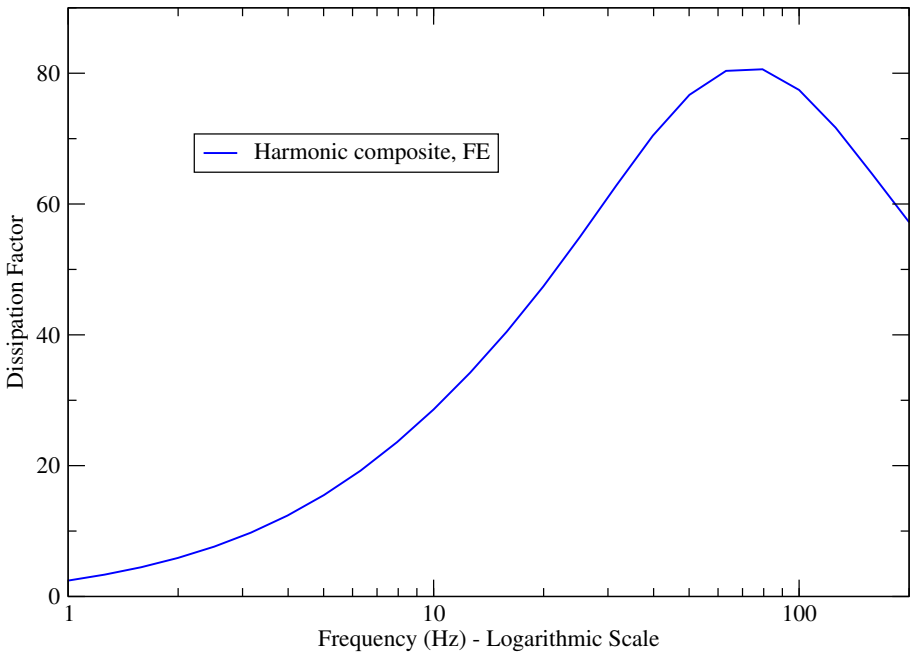

Figure 2. Effective P-wave dissipation factor as a function of frequency for the composite model. The numerical sample is a square of side length 18 cm and has seven alternating layers of ice contents $I' = 0.666$ and $I' = 0.166$.

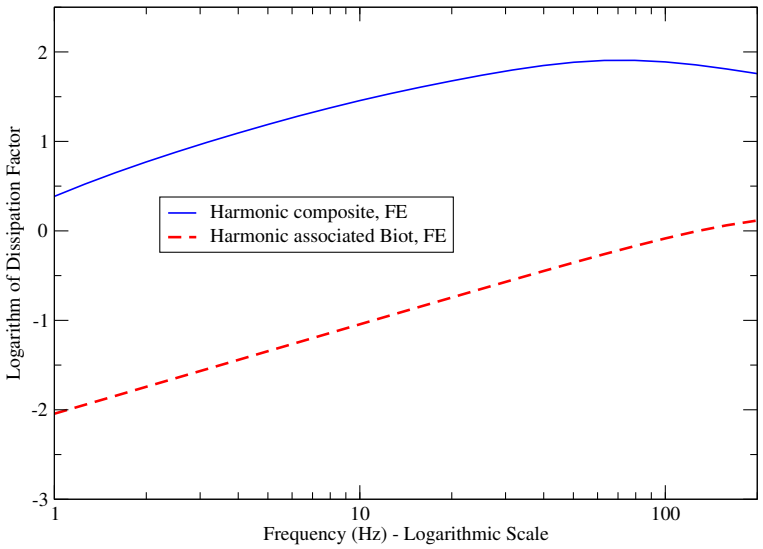

Figure 3. Logarithm of the effective P-wave dissipation factor as a function of frequency for the composite and associated classic Biot models. The numerical sample is a square of side length 18 cm and has seven alternating layers of ice content $I' = 0.666$ and $I' = 0.166$.

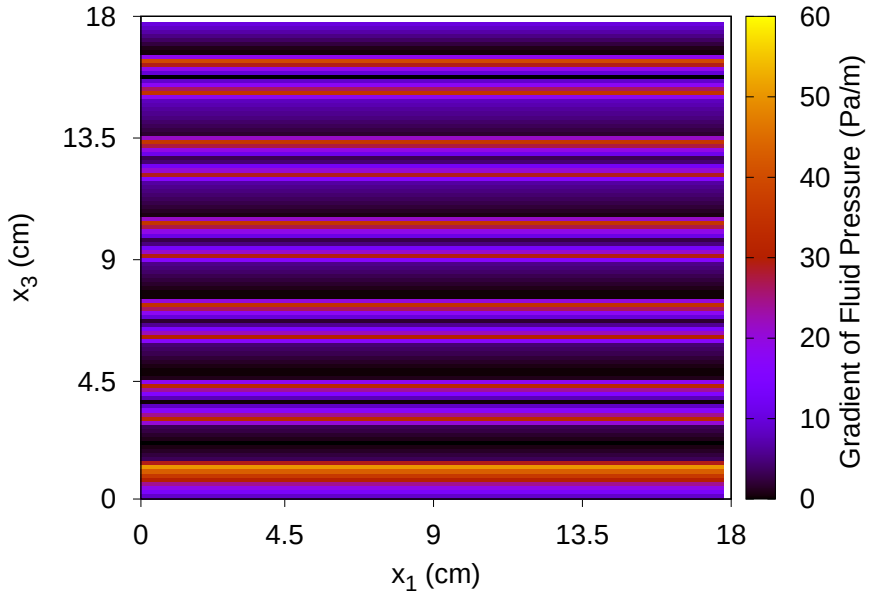

Figure 4. Gradient of fluid pressure at 10 Hz for a square numerical sample of side length 18 cm and with seven alternating layers of ice contents $I' = 0.666$ and $I' = 0.166$.

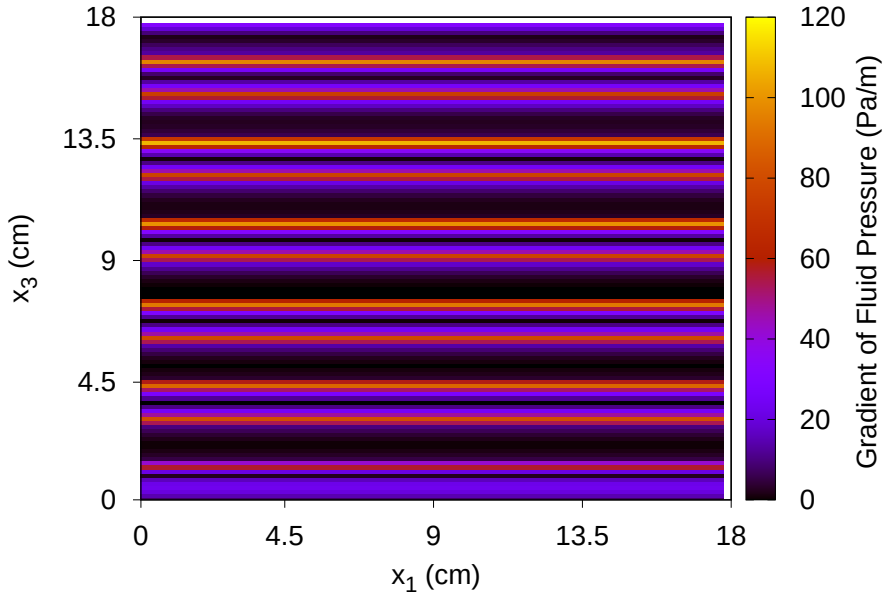

Figure 5. Gradient of fluid pressure at 70 Hz for a square numerical sample of side length 18 cm with seven alternating layers of ice contents $I' = 0.666$ and $I' = 0.166$.

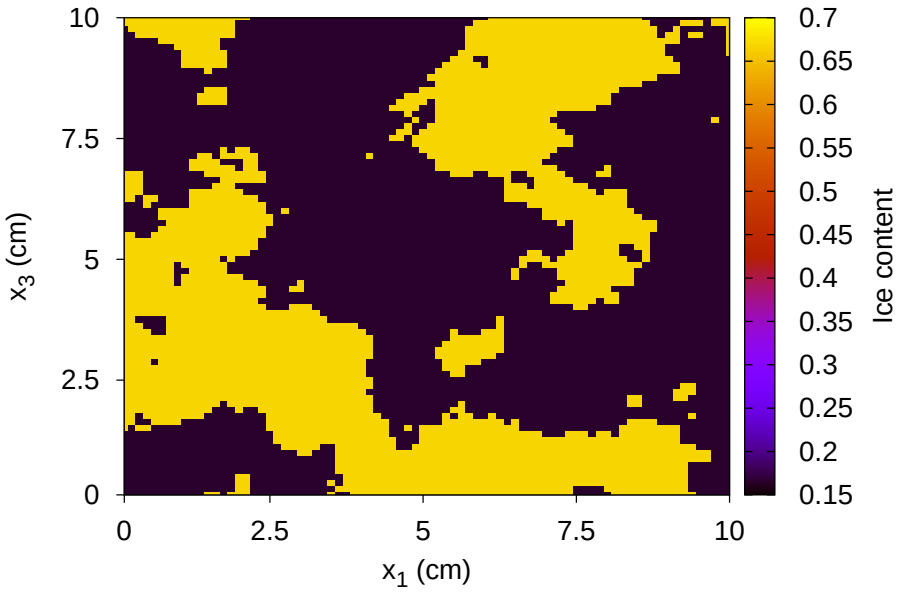

Figure 6. Binary patchy ice content I'. Black regions have $I' = 0.666$, yellow regions have $I' = 0.166$. Absolute porosity $\phi_a = 0.3$. Correlation length is 3.33 cm, fractal dimension is is $D = 2.22$. Overall ice content is 36 %. The sample is a square of side length 10 cm.

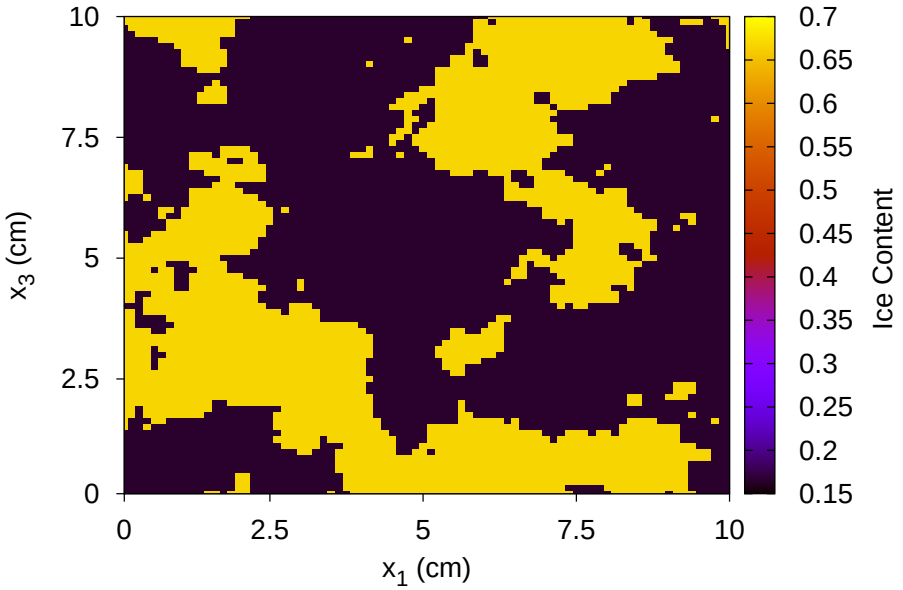

Figure 7. Binary patchy ice content I'. Black regions have $I' = 0.666$, yellow regions have $I' = 0.166$. Absolute porosity $\phi_a = 0.3$. Correlation length is 2.22 cm and fractal dimension is $D = 2.2$. Overall ice content is 36 %. The sample is a square of side length 10 cm.

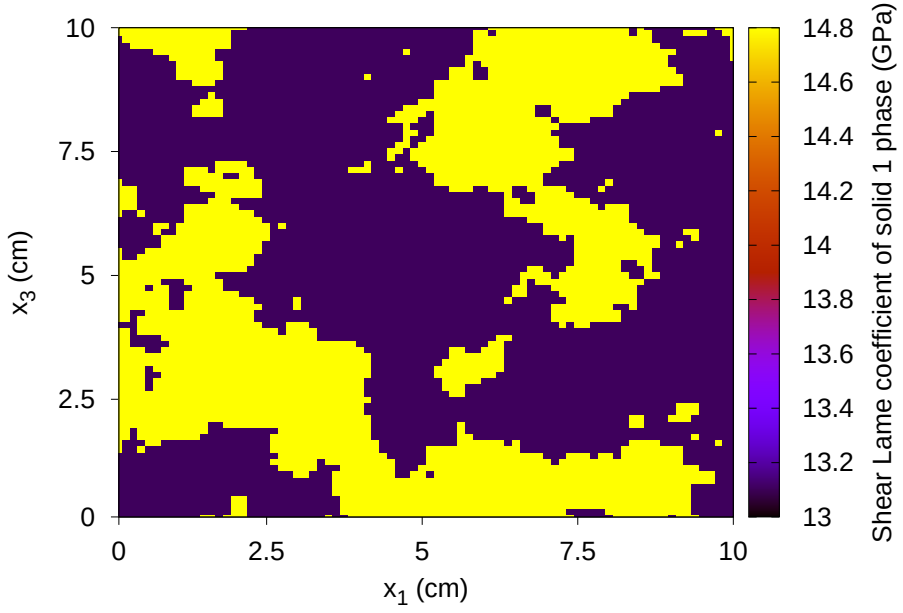

Figure 8. Lamé shear coefficient μ_1 associated with the binary patchy ice content of correlation length 2.22 cm and overall ice content is 36 %. The sample is a square of side length 10 cm.

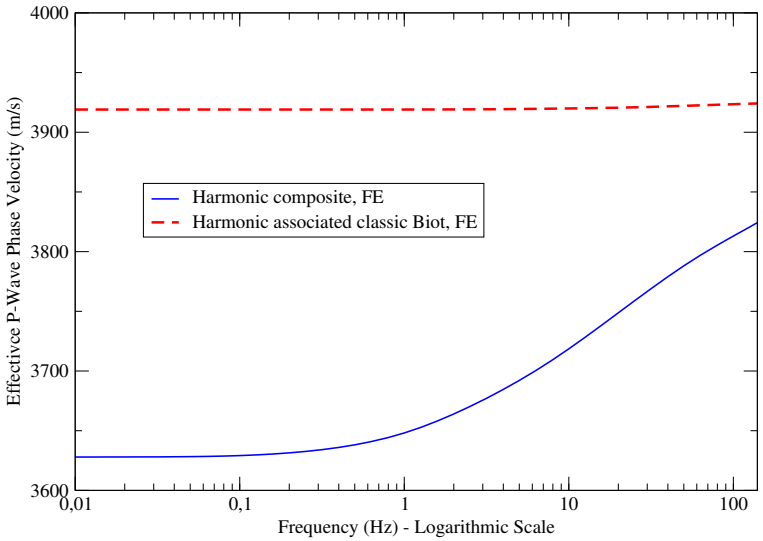

Figure 9. Effective P-wave phase velocity as a function of frequency for the composite and associated classic Biot models and fractal binary ice content I' as in Figure 7. Correlation length is 2.22 cm and Overall ice content is 36 %. The sample is a square of side length 10 cm.

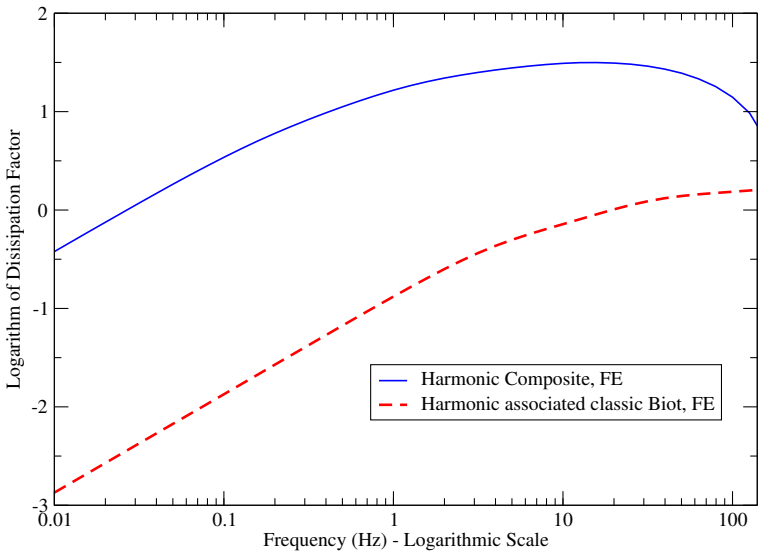

Figure 10. Effective P-wave dissipation factor as a function of frequency for the composite and associated classic Biot models and fractal binary ice content I' as in Figure 7. Correlation length is 2.22 cm and Overall ice content is 36 %. The sample is a square of side length 1 cm.

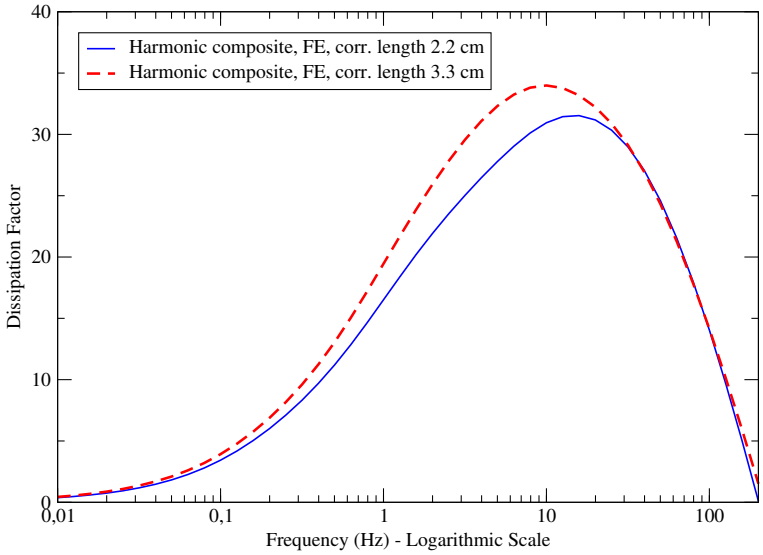

Figure 11. Effective P-wave dissipation coefficient as a function of frequency for the composite model and fractal binary ice content I' as in Figures 6 (Correlation length is 3.33) and 7 (Correlation length is 2.22). The attenuation peak moves to higher frequencies for the shorter correlation length. Overall ice content is 36 %. The sample is a square of side length 10 cm.

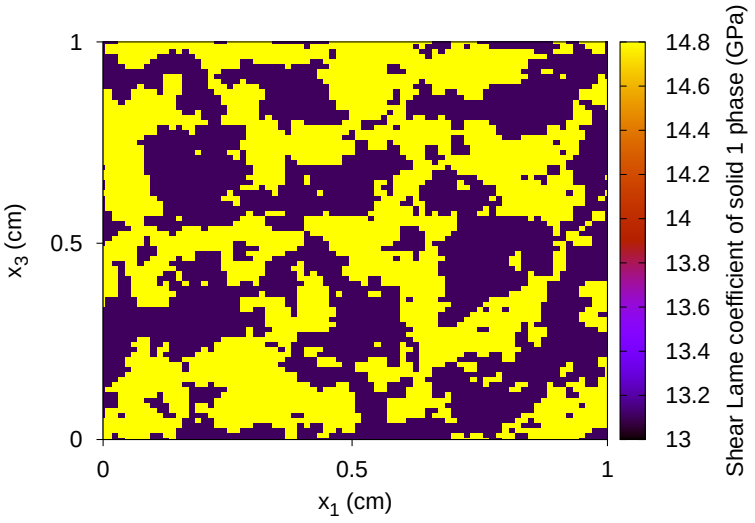

Figure 12. Lamé shear coefficient μ_1 associated with a binary patchy ice content of correlation length is 0.04 cm and overall ice content 41 %. The sample is a square of side length 1 cm.

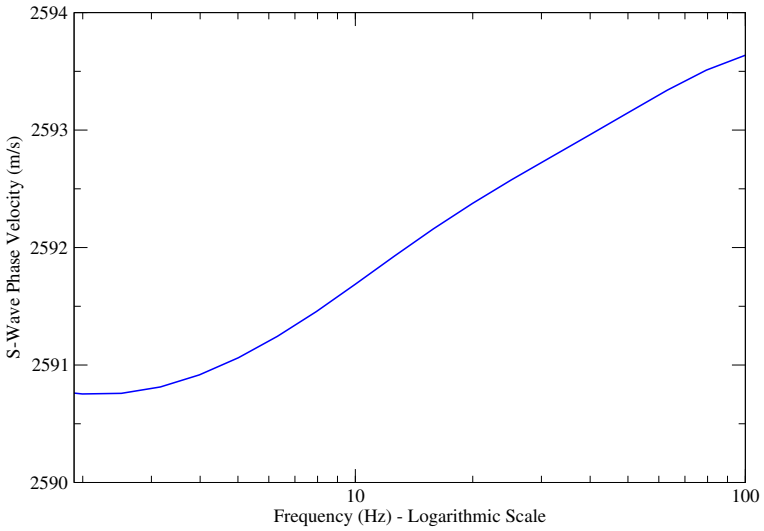

Figure 13. Effective S-wave phase velocity as function of frequency for the composite model and a binary patchy ice content of correlation length is 0.04 cm and overall ice content is 41 %. The sample is a square of side length 1 cm.